Performance calculation for single-sided linear induction motors with a solid steel reaction plate under constant current excitation

J.F. Gieras, Ph.D., D.Sc., Mem.I.E.E.E., A.R. Eastham, Ph.D., Sen.Mem.I.E.E.E., and G.E. Dawson, M.Sc., Ph.D., Mem.I.E.E.E.

Indexing terms: Induction motors, Linear Motors, Motors

Abstract: We present an analysis of the single-sided linear induction motor with a solid-steel reaction plate. By solving for the two-dimensional field distribution in the airgap and in the secondary, the mutual reactance and secondary impedance are determined. The saturable characteristics of the rail steel, together with the hysteresis, the skin effect, the reaction of eddy currents, and both transverse edge and longitudinal end effects are included. Computations for motoring and for plugging operation under constant-current conditions are compared with experimental results from a large-scale test linear machine, and good agreement is obtained. The analysis, which can also be used for constant-voltage excitation, is valid over a wide range of operating conditions, and is useful for design studies.

List of principal symbols

A = area, line current density
a_R = coefficient for resistance and active power losses, taking into account nonlinear magnetic permeability and hysteresis losses
a_x = coefficient for reactance and reactive power losses, taking into account nonlinear magnetic permeability and hysteresis losses
E = electric field strength
F = force
f = frequency, force per unit area
g = airgap
g' = equivalent airgap
H = magnetic field strength
I = electric current
k_c = Carter's coefficient
k_e = longitudinal end-effect factor
k_{trv} = factor for referring the secondary impedance to the primary
k_{wv} = primary winding factor
k_{zv} = transverse edge-effect factor
k_{vFe} = attenuation factor
k_μ = saturation factor
L = width of the primary stack
M_v = denominator in electromagnetic field equations
m = number of primary phases
N = number of turns per phase
P = active power
p = number of pole pairs
R = resistance
s = slip
t = time
V = MMF, magnetic potential drop
v = velocity
w = width of the secondary
X = reactance
Δx = increment of the primary core in the x-direction
Z = impedance
z = surface wave impedance
α_v = complex propagation constant

β_v = $v\pi/\tau$ = real constant
ε = EMF
η = efficiency
κ_v = complex propagation constant, dependent on the pole pitch
μ = magnetic permeability (μ_0 = permeability of free space, μ_r = relative, μ_{re} = relative equivalent, μ_{rs} = relative surface)
v = space harmonics of field distribution along the pole pitch
σ = electrical conductivity
τ = pole pitch
ϕ = phase angle (between current and voltage vectors)
ω = angular frequency

Subscripts

Fe = steel
m = peak values
$mech$ = mechanical
out = output
$prim$ = primary
sec = secondary
x, y, z = components along x-, y-, and z-co-ordinates, respectively

Superscripts

$+$ = forward-travelling field
$-$ = backward-travelling field

1 Introduction

After over twenty years of research and development, linear electric drives are now finding application in innovative transportation systems. The linear synchronous motor is favoured for high-speed applications: an air-core design is used for JNR's electrodynamically levitated test vehicle [1], while an iron-cored version provides propulsive power for the West German Transrapid electromagnetically suspended vehicle [2].

Linear induction motors are finding their first application in low-speed urban transit vehicles, such as the magnetically suspended Advanced Transit Shuttle Link now carrying passengers between Birmingham airport, Birmingham International railway station and the UK

National Exhibition Centre [3], and the steerable-axle trucked intermediate capacity transit system being installed in Vancouver, Scarborough and Detroit. Both vehicle systems use single-sided linear induction motors (SLIM), with an aluminium cap over the steel reaction rail in order to achieve the best electromechanical performance, i.e. adequate thrust at the highest power-factor-efficiency product (typically 0.35–0.45). An active track version of the linear induction drive is used in the Wedway People Mover in Orlando and at Houston airport [4].

Linear electric drives are essential for vehicles with non-contact suspension, and provide wheeled vehicles with propulsion that is independent of wheel-rail adhesion. This latter characteristic can be exploited in new transportation applications. The economics of such systems may favour the use of an inexpensive reaction rail, even though such a design may lead to a deterioration in electrical terminal characteristics. Hence there is interest in the use of a solid-steel reaction plate for SLIM drives. The authors have examined the feasibility of variable-voltage fixed-frequency (60 Hz) drives for low-speed shuttle vehicles [5], and other applications could include propulsion/braking 'helpers' for freight locomotives on steep grades and material handling shuttles in mines or factories. While the solid-steel rail LIM does not produce as great a peak thrust as a LIM with an aluminium-capped rail, one potentially useful feature is the shape of its thrust/speed characteristic. Under constant-current excitation, and at slip frequencies greater than about 10 Hz, the characteristic is almost flat [5–7], providing substantial thrust for acceleration and 'plug' braking at constant-frequency excitation.

In this paper, we present an analysis which takes into account the nonlinear saturation and hysteretic features of the solid ferromagnetic reaction plate, and which takes into account both transverse edge and longitudinal end effects.

2   Approaches to solid-steel rail slim analysis

The objective of the work reported here was to develop an analysis for a LIM with a solid-steel reaction plate which would serve as a design tool and which could accurately predict electrical and mechanical characteristics over a wide range of operating conditions.

The group at Queen's University has previously used a simple fundamental space harmonic model of the solid-steel rail SLIM [6], using the surface impedance concept and the Agarwal penetration depth of a time-varying field into a solid-steel plate [8]. This model was developed from an analysis of the solid-steel rotor induction motor [9]. It provides reasonable agreement with test results in the motoring régime, and is useful for the first iteration for machine design.

For detailed analysis of an induction machine with a solid iron secondary, it is necessary to evaluate the electromagnetic field distribution in the machine. While some attempts have been made to analyse the motor by finite-element or finite-difference techniques [for example, References 10–13], most authors have used either the multilayer approach [14–17] or a Fourier-series/transform representation of the fields [18–21]. A two-dimensional analysis allows the use of a single Fourier series (instead of the double series required for a three-dimensional problem) and simplifies the inclusion of magnetic saturation and hysteresis effects. The most sophisticated method of including variable magnetic permeability and hysteresis losses in solid iron is that presented by Nejman [22] and developed by later authors [23, 24].

In addition to accounting for the nonlinearity of the solid-iron reaction rail, both transverse edge and longitudinal end effects must be considered. Experimental studies [25, 26] have shown that longitudinal end effects are small for low-speed solid-steel rail LIM drives. Both transverse edge and longitudinal end effects can therefore be accounted for by correction factors. In this paper, it is shown that the LIM with a solid iron secondary can be analysed to good accuracy over a wide range of operating conditions by first considering the per-unit-area performance of a machine over a steel plate of constant permeability, and then by applying correction factors to account for nonlinearity, hysteresis, and saturation of the magnetic circuit, and for edge and end effects.

3   Electromagnetic field distribution in a SLIM with an infinite-length primary and secondary

As a first step towards the analysis of a finite-length SLIM with a solid-steel reaction rail, the field distribution of an infinite-length machine will be determined. The finite dimensions of the primary will then be included by transverse-edge-effect and longitudinal-end-effect factors.

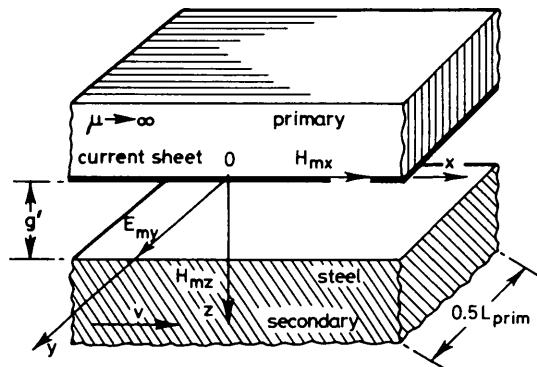With reference to Fig. 1, the Cartesian co-ordinate

Fig. 1   Model of SLIM with infinite length primary and secondary

system is fixed to the primary, which moves at a speed $v = v_s(1 - s)$ relative to the secondary. Equations for the two-dimensional electromagnetic field distribution in the airgap and secondary will be derived using the following assumptions:

(a) The primary core is composed of thin laminations with infinite magnetic permeability and with zero electric conductivity in the y-direction.

(b) The primary winding is represented by an infinitely thin current sheet containing the winding space harmonics.

(c) The region for electromagnetic field analysis consists of three isotropic layers; the first layer is a primary steel half space; the second layer is an airgap with thickness g', permeability μ_0 and zero conductivity; the third layer is a secondary steel half space.

(d) The active surface of the secondary is parallel to that of the primary.

(e) The relative equivalent magnetic permeability of the secondary ferromagnetic half space μ_{re} is given by the expressions

$$\mu_{re} = \mu_{rs}(\mu' - j\mu'') \tag{1}$$

$$\mu' = a_R a_x \tag{2}$$

$$\mu'' = 0.5(a_R^2 - a_x^2) \tag{3}$$

where the coefficients a_R, a_x are dependent on surface magnetic field strength, and take variable magnetic permeability and hysteresis into account [24].

(f) The equivalent magnetic permeability of the secondary ferromagnetic half space for higher field harmonics is the same as for the fundamental component.

(g) The primary and secondary currents flow only in the y-direction.

(h) The space period of electromagnetic field distribution in the x-direction is equal to 2τ.

(i) All quantities vary sinusoidally with time.

The equations for the two-dimensional electromagnetic field distribution have the following form [27]:

(i) For region 2, $0 < z < g'$

$$H_{mx2} = \sum_{v=1}^{\infty} \left\{ \frac{1}{M_v^+} \left[\frac{\kappa_{v1}^+}{\beta_v} \cosh \beta_v(z - g') \right. \right.$$
$$\left. - \mu_{re} \sinh \beta_v(z - g') \right] (-A_{mv}^+ e^{-j\beta_v x})$$
$$+ \frac{1}{M_v^-} \left[\frac{\kappa_{v1}^-}{\beta_v} \cosh \beta_v(z - g') \right.$$
$$\left. \left. - \mu_{re} \sinh \beta_v(z - g') \right] (-A_{mv}^- e^{j\beta_v x}) \right\} \quad (4)$$

$$H_{mz2} = \sum_{v=1}^{\infty} \left\{ \frac{1}{M_v^+} \left[\mu_{re} \cosh \beta_v(z - g') \right. \right.$$
$$\left. - \frac{\kappa_{v1}^+}{\beta_v} \sinh \beta_v(z - g') \right] jA_{mv}^+ e^{-j\beta_v x}$$
$$+ \frac{1}{M_v^-} \left[\mu_{re} \cosh \beta_v(z - g') \right.$$
$$\left. \left. - \frac{\kappa_{v1}^-}{\beta_v} \sinh \beta_v(z - g') \right] (-jA_{mv}^-)e^{j\beta_v x} \right\} \quad (5)$$

$$E_{my2} = \sum_{v=1}^{\infty} \left\{ \frac{1}{M_v^+} \left[\mu_{re} \cosh \beta_v(z - g') - \frac{\kappa_{v1}^+}{\beta_v} \sinh \beta_v(z - g') \right] \right.$$
$$\times \frac{j\omega\mu_0}{\beta_v} A_{mv}^+ e^{-j\beta_v x} + \frac{1}{M_v^-}$$
$$\times \left[\mu_{re} \cosh \beta_v(z - g') - \frac{\kappa_{v1}^-}{\beta_v} \sinh \beta_v(z - g') \right]$$
$$\left. \times \frac{j\omega\mu_0}{\beta_v} A_{mv}^- e^{j\beta_v x} \right\} \quad (6)$$

(ii) For region 1, $z \geqslant g'$

$$H_{mx1} = \sum_{v=1}^{\infty} \left[\frac{1}{M_v^+} \frac{\kappa_{v1}^+}{\beta_v} e^{-\kappa_{v1}^+(z - g')}(-A_{mv}^+ e^{-j\beta_v x}) \right.$$
$$\left. + \frac{1}{M_v^-} \frac{\kappa_{v1}^-}{\beta_v} e^{-\kappa_{v1}^-(z - g')}(-A_{mv}^- e^{j\beta_v x}) \right] \quad (7)$$

$$H_{mz1} = \sum_{v=1}^{\infty} \left[\frac{1}{M_v^+} e^{-\kappa_{v1}^+(z - g')}(jA_{mv}^+ e^{-j\beta_v x}) \right.$$
$$\left. + \frac{1}{M_v^-} e^{-\kappa_{v1}^-(z - g')}(-jA_{mv}^- e^{j\beta_v x}) \right] \quad (8)$$

$$E_{my1} = \sum_{v=1}^{\infty} \left[\frac{1}{M_v^+} e^{-\kappa_{v1}^+(z - g')} \frac{j\omega_v^+ \mu_0 \mu_{re}}{\beta_v} A_{mv}^+ e^{-j\beta_v x} \right.$$
$$\left. + \frac{1}{M_v^-} e^{-\kappa_{v1}^-(z - g')} \frac{j\omega_v^- \mu_0 \mu_{re}}{\beta_v} A_{mv}^- e^{j\beta_v x} \right] \quad (9)$$

where

$$M_v = \frac{\kappa_{v1}}{\beta_v} \cosh \beta_v g' + \mu_{re} \sinh \beta_v g' \quad (10)$$

$$g' = gk_c$$

$$\beta_v = v\pi/\tau \quad (11)$$

$$\kappa_{v1} = (\alpha_{v1}^2 + \beta^2)^{1/2} = (a_{RvFe} + ja_{xvFe})k_{vFe} \quad (12)$$

$$\alpha_{v1} = (j\omega_v \mu_0 \mu_{re} \sigma_{Fe})^{1/2} = (a_R + ja_x)k_{vFe} \quad (13)$$

$$k_{vFe} = (\omega_v \mu_0 \mu_{rs} \sigma_{Fe}/2)^{1/2} \quad (14)$$

$$a_{RvFe} = \mathrm{Re}\,[\kappa_{v1}]/k_{vFe} \quad (15)$$

$$a_{xvFe} = \mathrm{Im}\,[\kappa_{v1}]/k_{vFe} \quad (16)$$

$$A_{mv} = \frac{mNk_{wv}\sqrt{2I}}{p\tau} \quad (17)$$

Signs $^+$ and $^-$ correspond to forward and backward travelling fields, respectively. When the co-ordinate system moves with linear velocity v relative to the secondary, we have

(i) For forward-travelling fields, i.e. $v = 6k + 1$, where $k = 0, 1, 2, 3, \ldots$

$$\omega_v^+ = [1 - v(1 - s)]\omega = 2\pi f[1 - v(1 - s)] \quad (18)$$

(ii) For backward-travelling fields, i.e. $v = 6k - 1$, where $k = 1, 2, 3, \ldots$

$$\omega_v^- = [1 + v(1 - s)]\omega = 2\pi f[1 + v(1 - s)] \quad (19)$$

Time factors $\exp(j\omega_v^+ t)$ in A_{mv}^+, H_{mx}^+, H_{mz}^+, E_{my}^+, and $\exp(j\omega_v^- t)$ in A_{mv}^-, H_{mx}^-, H_{mz}^-, E_{my}^-, in eqns. 4–9 have been eliminated. For a three-phase winding ($m = 3$), the space-harmonics $v = 1, 7, 13, 19, \ldots$, of the line-current density wave A_{mv}^+ travel in the positive x-direction, while the space harmonics $v = 5, 11, 17, 23, \ldots$, of A_{mv}^- wave travel in the negative x-direction.

To calculate the Carter factor k_c, it is necessary to apply the exact formula derived by Carter [28, 29], because the airgap is usually greater than the slot opening. Simplified formulas do not give good results.

4 Secondary impedance

Unit surface impedance of the ferromagnetic secondary is given by the ratio of the tangential components of the electric field and the magnetic field

$$z_{yv} = \left. \frac{E_{myv}}{H_{mxv}} \right|_{z = g'} = -\frac{j\omega_v \mu_0 \mu_{re}}{\kappa_{v1}} \quad (20)$$

Multiplying expression 20 by vL/τ and by the edge-effect factor k_{zv} (see Appendix 16.1), we obtain the effective impedance of the secondary with finite dimensions. Impedance referred to the primary winding has the form

$$Z'_{vsec} = R'_{vsec} + jX'_{vsec}$$
$$= \mathrm{Re}\,[Z'_{vsec}] + j\,\mathrm{Im}\,[Z'_{vsec}]$$
$$= \frac{j\omega_v \mu_0 \mu_{re}}{\kappa_{v1}} v \frac{L}{\tau} k_{zv} k_{trv} \quad (21)$$

Note that κ_{v1} is complex, so that the secondary impedance retains real and imaginary components. The factor for referring the resistance and reactance of the secondary to the primary winding is given by

$$k_{trv} = 2m(Nk_{wv})^2/vp \quad (22)$$

where m = number of the primary phases, N = number of the primary-winding turns connected in series, k_{wv} = winding factor of the primary, and p = number of pole pairs.

5 Mutual impedance

The unit wave impedance, 'looking' from the primary into the region below the current sheet is

$$z_\nu = \left.\frac{E_{my2}}{H_{mx2}}\right|_{z=0}$$

$$= -\frac{j\omega\mu_0}{\beta_\nu}\frac{\mu_{re}\cosh\beta_\nu g' + \dfrac{\kappa_{\nu1}}{\beta_\nu}\sinh\beta_\nu g'}{\dfrac{\kappa_{\nu1}}{\beta_\nu}\cosh\beta_\nu g' + \mu_{re}\sinh\beta_\nu g'}$$

$$= z_{y\nu}\frac{\dfrac{\omega}{\omega_\nu}\cosh\beta_\nu g' - \dfrac{1}{z_{y\nu}}\dfrac{j\omega\mu_0}{\beta_\nu}\sinh\beta_\nu g'}{\cosh\beta_\nu g' - \dfrac{\omega}{\omega_\nu}\dfrac{\beta_\nu}{j\omega\mu_0}z_{y\nu}\sinh\beta_\nu g'} \quad (23)$$

This represents unit secondary impedance $z_{y\nu}$ in parallel with unit magnetising reactance $x_{Fe\nu}$. Dividing the numerator and the denominator of eqn. 23 by $z_{y\nu}$ and putting $z_{y\nu}\to\infty$, we obtain the unit reactance $x_{Fe\nu}$. Multiplying eqn. 23 by $\nu L/\tau$ and by $k_{tr\nu}$ from eqn. 22, the magnetising reactance has the following form:

$$X_{Fe\nu} = x_{Fe\nu}\nu\frac{L}{\tau}k_{tr\nu}$$

$$= \frac{\omega\mu_0}{\beta_\nu}\frac{1}{\tanh\beta_\nu g'}\nu\frac{L}{\tau}k_{tr\nu}$$

$$\approx 4mf\mu_0\frac{(Nk_{w\nu})^2}{vp}\frac{L}{\beta_\nu g'} \quad (24)$$

In addition to the Carter factor k_c the equivalent airgap g' in eqn. 24 should contain the saturation factor k_μ, so that

$$g' = gk_c k_\mu \quad (25)$$

where, under assumption (a)

$$k_\mu \simeq 1 + \frac{|V_{sec}|}{2|V_g|} \quad (26)$$

Formula 26 is valid for the fundamental space harmonic $v = 1$, where V_{sec} = magnetic potential drop across the secondary, and V_g = magnetic potential drop across the airgap (see Appendix 16.2).

The effective resistance in parallel with the magnetising reactance, representing active power losses in the primary core, is equal to

$$R_{Fe\nu} = \frac{m\varepsilon_\nu^2}{\Delta P_{Fe\nu}}k_{ad} \quad (27)$$

where ε_ν = EMF of the primary winding, $\Delta P_{Fe\nu}$ = eddy current and hysteresis losses in the primary core, k_{ad} = coefficient of additional losses in primary core. For LIMs, $k_{ad} = (1.2 - 2.0)$. As series rather than parallel elements, magnetising resistance and reactance become

$$R_{\mu\nu} = \frac{R_{Fe\nu}X_{Fe\nu}^2}{R_{Fe\nu}^2 + X_{Fe\nu}^2} \quad (28)$$

$$X_{\mu\nu} = \frac{R_{Fe\nu}^2 X_{Fe\nu}}{R_{Fe\nu}^2 + X_{Fe\nu}^2} \quad (29)$$

Mutual impedance in the 'vertical' branch of the LIM equivalent circuit is then

$$Z_{\mu\nu} = R_{\mu\nu} + jX_{\mu\nu} \quad (30)$$

6 Equivalent circuit for fundamental space harmonic

The per-phase equivalent circuit for $v = 1$ and for negligible longitudinal end effect is shown in Fig. 2. The RMS
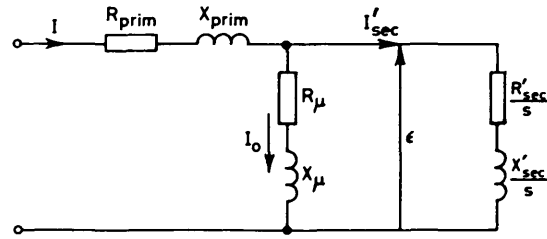

Fig. 2 *Equivalent circuit of SLIM for the first space harmonic ($v = 1$), without longitudinal end effect*

secondary current, referred to the primary winding, is given by

$$I'_{sec} = \frac{s\varepsilon}{\sqrt{(R'_{sec})^2 + (X'_{sec})^2}} = \frac{\varepsilon}{\sqrt{\left(\dfrac{R'_{sec}}{s}\right)^2 + \left(\dfrac{X'_{sec}}{s}\right)^2}} \quad (31)$$

where ε = EMF induced in primary winding (airgap voltage), and s = slip of the secondary relative to the fundamental space harmonic of magnetic field produced by the primary winding.

The RMS current in the mutual branch of the equivalent circuit reduced to the primary winding is equal to

$$I_0 = \frac{\varepsilon}{\sqrt{(R_\mu^2 + X_\mu^2)}} \quad (32)$$

Total input current I is the phasor sum of secondary current I'_{sec} and current I_0. For constant current excitation, the ratio I'_{sec}/I_0 depends only on Z_μ/Z'_{sec}. The resistance and leakage reactance of the primary winding may be calculated as in rotating induction machines. Electromagnetic power transferred from the primary to the secondary is

$$P_{e/m} = \frac{m(I'_{sec})^2 R'_{sec}}{s} \quad (33)$$

Mechanical power is then

$$P_{mech} = P_{e/m}(1 - s) \quad (34)$$

Efficiency is

$$\eta = \frac{P_{out}}{P_{e/m} + \Delta P_{prim}} = \frac{P_{out}}{P_{in}} \quad (35)$$

where ΔP_{prim} = active power losses in the primary core and winding, and P_{in} = input power.

The power factor is calculated as $\cos\phi = R_t/|Z_t|$, where R_t = total effective resistance, and $|Z_t|$ = absolute value of total impedance of the equivalent circuit.

7 Thrust force

The thrust force F_x is equal to the electromagnetic power (eqn. 33) divided by the synchronous velocity $v_s = 2\tau f$, i.e.

$$F_x = \frac{P_{e/m}}{v_s} = \frac{m(I'_{sec})^2 R'_{sec}}{sv_s} \quad (36)$$

The edge effect is included in resistance R'_{sec} by the factor k_z (see Appendix 16.1), and the end effect may be included

by modifying the secondary current

$$I'_{sec} = \frac{(1 - k_e)I \dfrac{Z_\mu Z'_{sec}}{|Z_\mu + Z'_{sec}|}}{|Z'_{sec}|} \qquad (37)$$

where the factor k_e is dependent on slip, as discussed in Appendix 16.3.

8 Normal force

As with thrust, the normal force derived directly from the electromagnetic field equations does not provide a good correlation with test results. We have obtained analytical results which are very close to measurements by applying the following formula:

$$F_z = \frac{B_{mg}^2}{4\mu_0} A - \frac{B_{mx}}{B_{mg}} F_x \qquad (38)$$

where F_x is given by eqn. 36, and B_{mx} is given by eqn. 4. Eqn. 38 takes both the eddy current reaction and the end effect into account because B_{mg} is evaluated by use of eqn. 50 in Appendix 16.3. In eqn. 38, the equivalent area A of the primary is equal to

(i) When the secondary width $w < L + 2g'$

$$A = (2p\tau + \Delta x)w \qquad (39)$$

(ii) When the secondary width $w > L + 2g'$

$$A = (2p\tau + \Delta x)(L + 2g') \qquad (40)$$

The additional dimension $\Delta x \neq 0$ when the length of the primary core in the x-direction is greater than $2p\tau$.

9 Experimental machine

In order to validate this analytical approach for performance calculation of a SLIM with a solid-steel reaction rail, the computed performance was compared with test results on a large-scale LIM using the Canadian Institute of Guided Ground Transport (CIGGT) test facility at Queen's University. The test facility uses a 7.6 m (25 ft) diameter rotating wheel to provide relative motion between rim-mounted guideway components (the solid-steel reaction rail) and a stationary vehicle module (the linear induction motor). The CIGGT test wheel and detail of the LIM and reaction rail configuration are shown in Fig. 3.

Design data for the LIM, used as input parameters for performance computation, are listed in Table 1. The primary core is made of cold-rolled silicon nonoriented steel (M19) 0.318 mm thick and with an insulation factor of 0.96. From manufacturer's data, the unit power loss at $B = 1$ T and $f = 60$ Hz is 0.65 W/kg. The LIM was excited by a 200 kVA pulse-width-modulated inverter drive.

The mild-steel reaction rail was procured in ten 2.4 m long $\times$ 178 mm wide $\times$ 25 mm thick sections, each rolled to a curvature that matched that of the test wheel rim. Individual sections were joined by full-depth welding. The width of the reaction rail was subsequently reduced to 111 mm. The magnetisation curve was experimentally determined, and corresponding points and coefficients are given in Table 2.

The LIM was mounted in a six-component force balance, allowing thrust, normal and lateral forces, together with pitch, roll and yaw moments, to be measured. A PDP 11/03-based 64 channel data acquisition and processing system was used to measure the electrical input
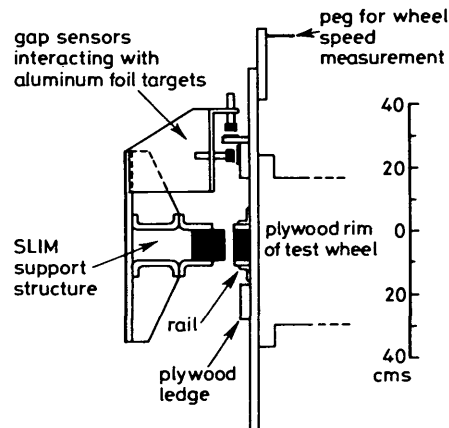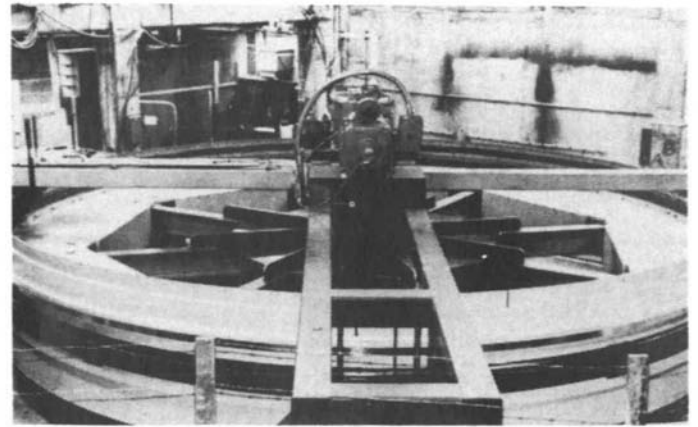

Fig. 3 *A general view and rim schematic of the 7.6 m diameter, 0–101 km/h CIGGT test wheel*

Table 1: Data for CIGGT experimental machine

Number of phases	$m = 3$
Number of pole pairs	$p = 3$
Nominal RMS input current	$I = 200$ A
Number of primary series turns per phase	$N = 108$
Diameter of primary wire	1.155 mm
Number of parallel wires per turn	19
Length of one side of end connection of single primary coil	0.2955 m
Primary coil pitch	0.1944 m
Width of primary core (in y-direction)	$L = 0.101$ m
Pole pitch	$\tau = 0.25$ m
Δx (eqns. 39 and 40)	0.23 m
Nominal airgap	$g = 15$ mm
Number of primary slots in $2 p\tau$	$z = 54$
Number of half-filled slots in Δx	7
Width of primary slot	15 mm
Height of primary slot	30.0 mm
Number of primary winding layers	2
Height of primary yoke	71.6 mm
Electric conductivity of solid secondary at 20°C	$\sigma_{Fe} = 4.46 \times 10^6$ S/m
Secondary width	$w = 0.111$ m
Thickness of secondary	25.4 mm

Table 2: Magnetisation curve and coefficients for the solid-steel secondary

H_{msFe} A/m	B_{mFe} Tesla	a_R	a_x
100	0.014	0.84	0.94
350	0.75	0.90	0.90
1000	1.15	1.61	0.93
2000	1.35	1.72	0.80
4000	1.475	1.61	0.78
6000	1.51	1.56	0.80
10000	1.53	1.52	0.82
16000	1.55	1.49	0.85
100000	1.81	1.45	0.94
1000000	1.90	1.38	0.98

(phase voltages and currents, frequency), position (airgap and lateral offset), mechanical output (forces, speed), and magnetic state of the machine at a number of positions in the primary and along the airgap. Sampled periodic signals were digitally filtered and scaled to yield RMS values of fundamental components, and sampled steady signals were averaged and scaled

10   Computations

The magnetic properties of the solid-steel reaction rail were specified by points in a look-up table, giving the magnetisation curve $B_{mFe}(H_{msFe})$ and including the coefficients $a_R(H_{msFe})$, $a_x(H_{msFe})$ which take into account the nonlinearity and hysteresis of the ferromagnetic rail. By assumption (a), we have excluded the magnetisation characteristic of the primary core. However, the primary-core losses are accounted for and are expressed as

$$\Delta p_{Fe} = (C_H + C_{EC} f)f B^2 k_{ad}$$

where C_H = hysteresis loss constant, C_{EC} = eddy current loss constant, f = frequency, B = flux density of the tooth or the yoke, k_{ad} = coefficient of additional losses in the primary core.

Magnetic field strength at the secondary surface is taken as

$$H_{msFe} = (|H_{mx1}|^2_{z=g'} + |H_{mz1}|^2_{z=g'})^{1/2} \qquad (41)$$

Our Fortran program executes the electromagnetic computations. First, all slip-independent parameters are calculated. For a given frequency and speed, computation is started for the no-load slip s_0. Initially, H_{msFe} is taken to be equal to the line current density of the primary A_m, according to eqn. 17 for $v = 1$. This represents the highest value (for zero slip) and, after computation of the electromagnetic field distribution and impedances of the equivalent circuit, H_{msFe} is iteratively brought to its correct value for any finite slip. The most appropriate value of relaxation factor for H_{msFe} was found to be 1.0, and the iteration was pursued until the change in H_{msFe} between successive iterations was less than 0.1%. Typically, the time of computation for twelve values of slip was 20 s using a VAX-11/750 digital computer.

11   Influence of higher space harmonics on thrust and normal forces

The influence of higher space harmonics on thrust and normal forces of the large airgap ($g' = 10–15$ mm) LIM with distributed and chorded windings was found to be very small, due to the high value of the attenuation factor k_{vFe}. Table 3 shows the thrust for the CIGGT machine (see

Table 3: Thrust for the CIGGT LIM due to higher space harmonics (for f = 18 Hz, I = 200 A and g = 15 mm)

v	k_{wv}	$\dfrac{F_{xv}}{F_{xv=1}}$, %	
		$s = 0.5$	$s = 1.0$
1	0.902	100.0000	100.0000
5	0.038	−0.0116	−0.0060
7	−0.136	−0.0500	0.0300
11	−0.136	−0.0215	−0.0084
13	−0.038	−0.0009	0.0004
17	0.902	−0.3171	−0.1190
19	−0.902	−0.2161	0.0906
23	0.038	−0.0003	−0.0001
25	0.136	−0.0025	0.0011
	Total	99.3792	99.9919

Table 1) calculated from the equivalent circuit, for fundamental ($v = 1$) and for higher space harmonics. The higher space harmonic fields are very strongly damped as compared with the fundamental field inside the solid ferromagnetic rail.

The influences of excitation time harmonics, produced by a variable frequency inverter, and phase unbalance in the solid-steel rail LIM were the subject of a follow-on investigation (to be published). Both were found to be small effects.

12   Comparison with test results

The computed and experimental thrust and normal forces as a function of speed at input current $I = 200$ A, reaction plate width $w = 111$ mm and airgap $g = 15$ mm at discrete frequencies over the range 5–40 Hz are shown in Figs. 4 and 5. Power input and the power-factor/efficiency
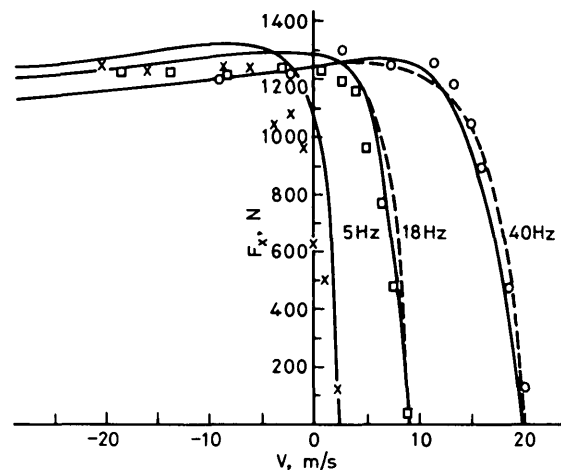
Fig. 4   *Thrust at 5 Hz, 18 Hz and 40 Hz as a function of speed, at $I = 200$ A, airgap $g = 15$ mm, and secondary width $w = 0.111$ m*

——— calculations with end effects
– – – – calculations without end effects
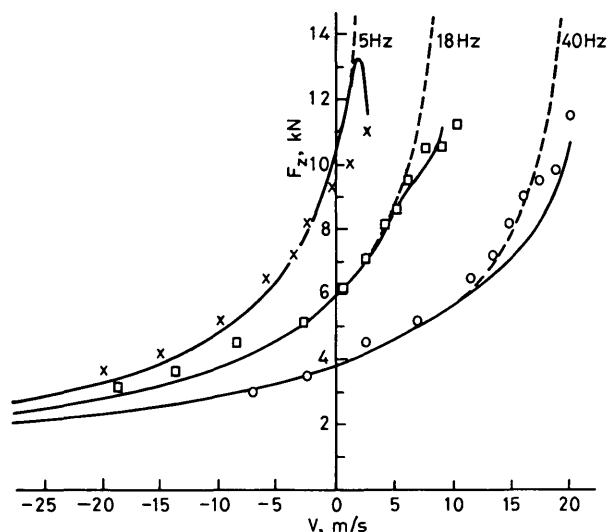experimental points: ×5 Hz, □ 18 Hz, ○ 40 Hz

Fig. 5   *Normal force at 5 Hz, 18 Hz and 40 Hz as a function of speed, at $I = 200$ A, $g = 15$ mm, and $w = 0.111$ m*

——— calculations with end effects
–.– – – calculations without end effects
experimental points: ×5 Hz, □ 18 Hz, ○ 40 Hz

product as a function of speed at 18 Hz, 200 A and 15 mm are shown in Figs. 6 and 7. Good agreement between analysis and test results is evident.

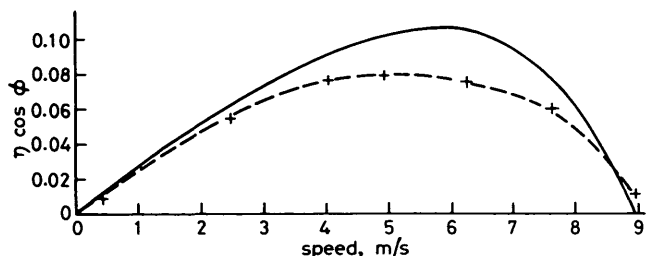The usefulness of an analytical technique is determined

190

Fig. 6 Power-factor/efficiency product (η cos ϕ) as a function of speed, at f = 18 Hz, I = 200 A, g = 15 mm, and w = 0.111 m
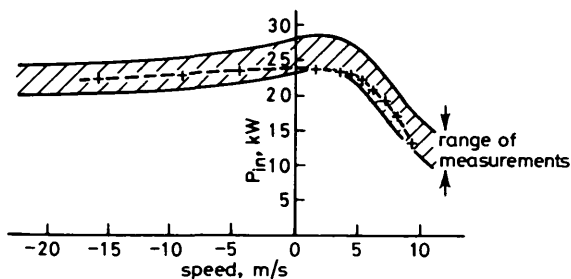
——— calculations, —+— measurements

Fig. 7 Power input to the SLIM as a function of speed, at f = 18 Hz, I = 200 A, g = 15 mm and w = 0.111 m
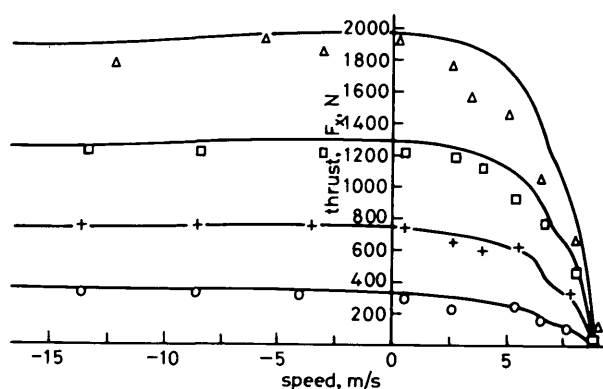
+ calculations

Fig. 8 Thrust at I = 100 A, 150 A, 200 A and 250 A as a function of speed at f = 18 Hz, g = 15 mm and w = 0.111 m
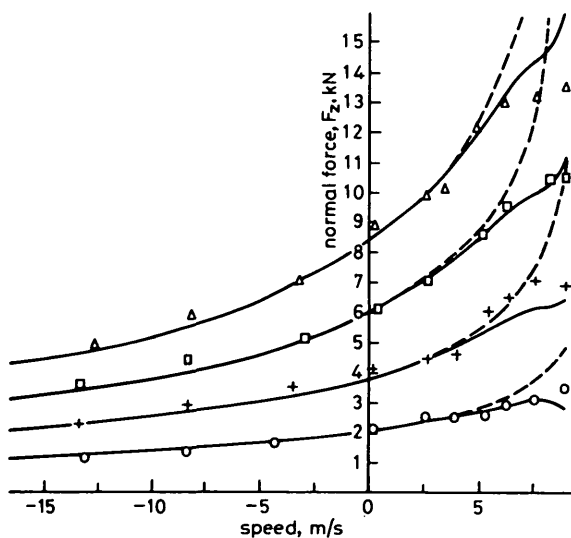
——— calculation ○ 100 A, +150 A, □ 200 A, △ 250 A

Fig. 9 Normal force at I = 100 A, 150 A, 200 A and 250 A as a function of speed at f = 18 Hz, g = 15 mm and w = 0.111 m

——— calculations with end effect; – – – – calculations without end effect; ○ 100A, +150 A, □ 200 A, △ 250 A

by its ability to accurately predict the performance of a machine over a wide range of operating conditions. Too often, correlation between test and theory is given for a very limited range of conditions. The influence of the primary current on thrust and normal forces (at 18 Hz and 15 mm gap) and the influence of airgap on thrust and normal forces (at 18 Hz and 200 A) are presented in Figs. 8–11. It is evident that, under constant-current excitation,
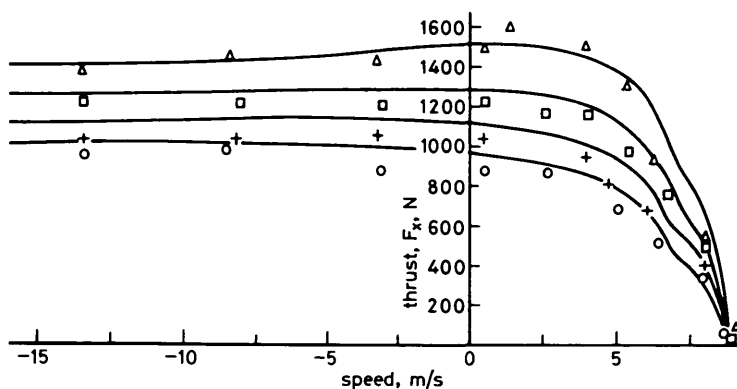

Fig. 10 Thrust at various gaps as a function of speed at f = 18 Hz, I = 200 A and w = 0.111 m
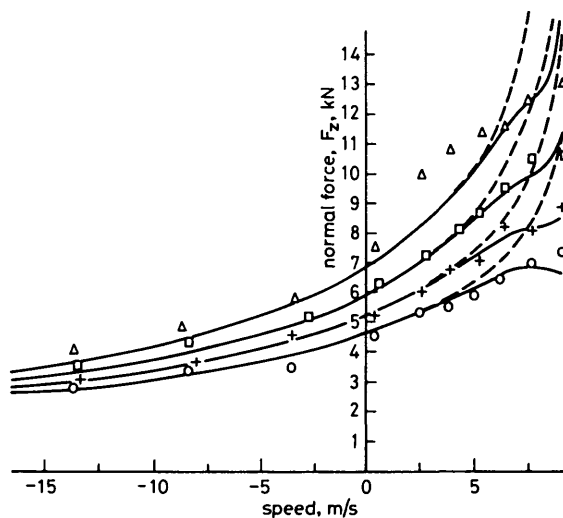
△ 12.5 mm, □ 15.0 mm, +17.5 mm, ○ 20.0 mm

Fig. 11 Normal force at various gaps as a function of speed at f = 18 Hz, I = 200 A and w = 0.111 m

——— calculations with end effect, – – – – calculations without end effect; △ 12.5 mm, □ 15.0 mm, +17.5 mm, ○ 20.0 m

both thrust and normal forces are sensitive to airgap and that this variation can be computed with good accuracy.

13 Conclusions

The performance of a linear induction motor is generally thermally limited by the RMS current that the primary can carry over its operational cycle. It is more difficult to compute the performance of a SLIM under constant-current excitation than under constant-voltage conditions, particularly in the case of a solid-steel reaction plate without the addition of a high-conductivity cap. Many of the published analytical techniques become impractical when the LIM carries a high equivalent surface current density, causing deep saturation near the surface of the steel rail. Expressions for thrust and normal forces obtained from electromagnetic field theory alone often give errors as great as 100%. It is, in general, much more accurate to use an equivalent-circuit representation of the LIM, including corrections for edge and end effects and for mag-

netic saturation. Of course, the basic secondary impedance must still be evaluated from the electromagnetic field distribution.

It has been shown that the equivalent-circuit approach can predict the performance of a single-sided LIM with a solid-steel reaction rail over a wide range of operational conditions, including variable frequency, current and airgap. We emphasise here the importance of knowing and modelling the nonlinearity of the ferromagnetic reaction plate, and we have presented a means of determining the influence of this characteristic on airgap flux density EMF and mutual reactance of the LIM.

Having taken into account the nonlinearity of the solid steel, saturation of the magnetic circuit, the transverse edge effect and, less importantly for a steel rail with resistivity much greater than that of an aluminium cap, the longitudinal end effect, and having shown that good agreement is achieved between analysis and test results on a large scale LIM, the authors consider that the method presented here provides an effective tool for the design and performance calculation of a SLIM with a solid-steel reaction rail.

14 Acknowledgments

15 References

1 OHTSUKA, T., and KYOTANI, Y.: 'Recent progress in superconducting magnetic levitation tests in Japan'. Proc. IEEE IAS Annual Meeting, 1980, IEEE Publ. 80CH1575-0, pp. 238–243

2 GLATZEL, U., KHURDOCK, G., and ROGG, D.: 'The development of the magnetically suspended transportation system in the Federal Republic of Germany', IEEE Trans., 1980, VT-29, pp. 3–16

3 LINACRE, H., CHAHAL, J.S., CRAWSHAW, G., and RAWLINSON, B.: 'Birmingham airport Maglev propulsion system'. Proc. International Conference 'Maglev transport—now and for the future'. Solihull, October 9–10, 1984, I.Mec.E. 1984-12, pp. 192–201

4 TURNER, D.B., and WOLF, W.L.: 'Houston WEDWAY People Mover control and propulsion system'. Proc. 32nd IEEE vehicular technology conference, San Diego, May 1982

5 EASTHAM, A.R., DAWSON, G.E., JOHN, V.I., KAMAR, A.M.A., SEN, P.C., and WALLACE, A.K.: 'Voltage-controlled 60 Hz linear induction motor drives', Electr. Mach. & Power Syst., 1983, 8, pp. 487–497

6 DAWSON, G.E., WALLACE, A.K., EASTHAM, A.R., and KAMAR, A.M.A.: 'Design study of a LIM with a solid steel reaction rail for urban transit'. Proc. international conference on electric machines (ICEM 82), Budapest, September 1982, pp. 992–995

7 BOLOPIAN, A., and POLOUJADOFF, M.: 'The effect of using solid iron in the secondary of linear induction machines', Electr. Mach., 1983, 8, pp. 333–340

8 AGARWAL, P.D.: 'Eddy current losses in solid and laminated iron', Trans. AIEE, 1959, 78, pp. 169–181

9 PENMAN, J., and KAMAR, A.M.A.: 'Performance calculations for induction machines with a solid steel rotor', Electr. Mach. & Electromech., 1980, 5, pp. 509–521

10 NASAR, S.A., and DEL CID, L.: 'Certain approaches to the analysis of single-sided linear induction motors', Proc. IEE, 1973, 120, (4), pp. 477–483

11 NASAR, S.A., and BOLDEA, I.: 'Linear motion electric machines'. (J. Wiley, New York, 1976)

12 ALWASH, J.H.H., and AL-RIKABI, Y.A.H.: 'Finite-element analysis of linear induction machines', Proc. IEE, 1979, 126, (7), pp. 677–682

13 PENMAN, J., CHALMERS, B.J., KAMAR, A.M.A., and TUNCAY, R.N.: 'The performance of solid steel secondary linear induction motors', IEEE Trans., 1981, PAS-100, pp. 2917–2935

14 FREEMAN, E.M.: 'Travelling waves in induction machines: input impedance and equivalent circuits', Proc. IEE, 1968, 115, (12), pp. 1772–1776

15 LIPKIS, R.S., and WANG, T.C.: 'Single-sided linear induction motor (SLIM): a study of thrust and lateral forces'. TRW Systems Group, final report, 1971, McLean, Virginia

16 BOLDEA, I., and BABESCU, M.: 'Multilayer approach to the analysis of single-sided linear induction motors', Proc. IEE, 1978, 125, (4), pp. 283–287

17 BOLDEA, I., and NASAR, S.A.: 'Improved performance of high-speed single-sided linear induction motors: a theoretical study', Electr. Mach. & Electromech., 1978, 2, pp. 155–166

18 WOOD, A.J., and CONCORDIA, C.: 'An analysis of solid rotor machines, part III: finite length effects', Trans. AIEE, 1960, PAS-79, pp. 21–26

19 ANGST, G.: 'Polyphase induction motor with solid rotor: effects of saturation and finite length', ibid., 1962, PAS-81, pp. 902–909

20 OKHREMENKO, N.M.: 'Magnetic field of flat induction pump', Elektrichestvo, 1964, 8, pp. 18–26 (in Russian)

21 LASOCINSKI, T.: 'Electromagnetic field in airgap of machine with solid ferromagnetic rotor including finite length of machine', Rozpr. Elektrotech., 1966, 12, pp. 69–92 (in Polish)

22 NEJMAN, L.R.: 'Skin effect in ferromagnetic bodies'. GEI, Leningrad, Moscow, 1949 (in Russian)

23 TUROWSKI, J.: 'Calculation method of field and secondary performances of linear induction motors', Rozpr. Elektrotech., 1973, 19, pp. 371–396 (in Polish)

24 GIERAS, J.: 'Analytical method of calculating the electromagnetic field and power losses in ferromagnetic halfspace, taking into account saturation and hysteresis', Proc. IEE, 1977, 124, (11), pp. 1098–1104

25 NONAKA, S., and HIGUCHI, T.: 'Design principle of high speed single-sided linear induction motors for propulsion of magnetically levitated trains', Electr. Eng. Jpn., 1981, 101, pp. 96–105

26 NONAKA, S., and HIGUCHI, T.: 'Approximate equations for calculation of characteristics of single-sided linear induction motors', ibid., 1982, 102, pp. 18–25

27 GIERAS, J.: 'Elements of electromagnetic theory of induction machines'. D.Sc. Thesis, Zeszyty Naukowe ATR, Bydgoszcz, 1979 (in Polish)

28 CARTER, F.W.: 'The magnetic field of the dynamo-electric machine', J. IEE, 1926, 64, pp. 1115–1138

29 HELLER, B., and HAMATA, V.: 'Harmonic field effect in induction machines' (Elsevier Scientific Publishing Company, Amsterdam, 1977)

30 GIBBS, W.J.: 'Theory and design of eddy current slip couplings: II', BEAMA J., 1946, 53, pp. 123, 172–177, 219

31 RUSSELL, R.L., and NORSWORTHY, K.H.: 'Eddy currents and wall losses in screened-rotor induction motors', Proc. IEE, 1958, 105A, pp. 163–175

32 BOLTON, H.: 'Transverse edge effects in sheet-rotor induction motors', ibid., 1969, 116, (5), pp. 725–731

33 PANASIENKOV, M.A.: 'Electromagnetic calculations of devices with nonlinear distributed parameters', Energia, Moscow, 1971 (in Russian)

34 YEE, H.: 'Effects of finite length in solid-rotor induction machines', Proc. IEE, 1971, 118, (8), pp. 1025–1033

35 HIRASA, T., ISHIKAWA, S., and YAMAMURO, T.: 'Equivalent circuit of linear induction motors with end effect taken into account', Electr. Eng. Jpn., 1980, 100, pp. 65–71

36 YAMAMURA, S.: 'Theory of linear induction motors' (University of Tokyo Press, 1972)

16 Appendix

16.1 Edge-effect factor

Eqns. 4–9 were derived under assumption (g), i.e. that the electric field strength in the reaction rail has an E_{my} component only. In practice, the paths of the secondary eddy currents must close, and an E_{mx} component of electric field strength must exist. It is necessary to include the effect of eddy currents along the x-axis as these have an important influence on the secondary impedance. Many methods for treating transverse edge effects have been proposed [30–34]. The authors consider that the following formulas give the most useful correction factors for a LIM with a solid-steel reaction plate:

(i) according to Gibbs ($v = 1$) [30]

$$k_z = 1 + \frac{2}{\pi} \frac{\tau}{w} \tag{42}$$

(ii) according to Panasienkov ($v = 1$) [33]

$$k_z = 1 + 0.5 \frac{\tau}{w} \qquad (43)$$

(iii) according to Yee ($v = 1$) [34]

$$k_{zv} = \frac{\beta_{v=1} w \left[1 + \coth \left(\beta_{v=1} \dfrac{w}{2} \right) \right]}{\beta_{v=1} w \left[1 + \coth \left(\beta_{v=1} \dfrac{w}{2} \right) \right] - 2} \qquad (44)$$

(iv) proposed by one of the authors

$$k_{zv} = 1 - \frac{g}{vL} + \frac{2}{v\pi} \frac{\tau}{w} \left[1 - \exp \left(-v \frac{\pi}{2} \frac{w}{L} \right) \right] \qquad (45)$$

This latter expression was developed from an empirical determination of the field distribution in the edge region of a single-sided LIM. If $g \ll L$ and $w > L$, the expressions 45 and 42 take the same form. If $w > L + \tau$, we should put $L + \tau$ instead of w into expressions 42–45. Edge-effect factors according to expressions 42–45 are plotted as a function of reaction plate width w in Fig. 12.

Noting that $L < w < L + \tau$ for a practical SLIM design, and noting the difficulty of deriving a generally applicable analytical expression for edge correction, the authors propose to use the arithmetic mean of the above four edge-effect factors just mentioned as the value for SLIM analysis.

16.2 Saturation factor

In the classical theory of electrical machines, the saturation factor of the magnetic circuit is defined as the ratio of total MMF per pole pair to airgap MMF per pole pair. For induction machines with laminated cores (both primary and secondary), the saturation factor takes its maximum value at no load. When an induction machine has a solid-steel secondary, an increase in slip causes an increase in the tangential component of the magnetic field strength at the secondary surface. Consequently, the highest values of saturation factor occur in plugging operation ($s > 1$). As a result of the assumed very high magnetic permeability of the primary core (assumption (a)) and the lower saturation flux density of the solid secondary than of the primary core, the MMF of the primary core may be neglected and
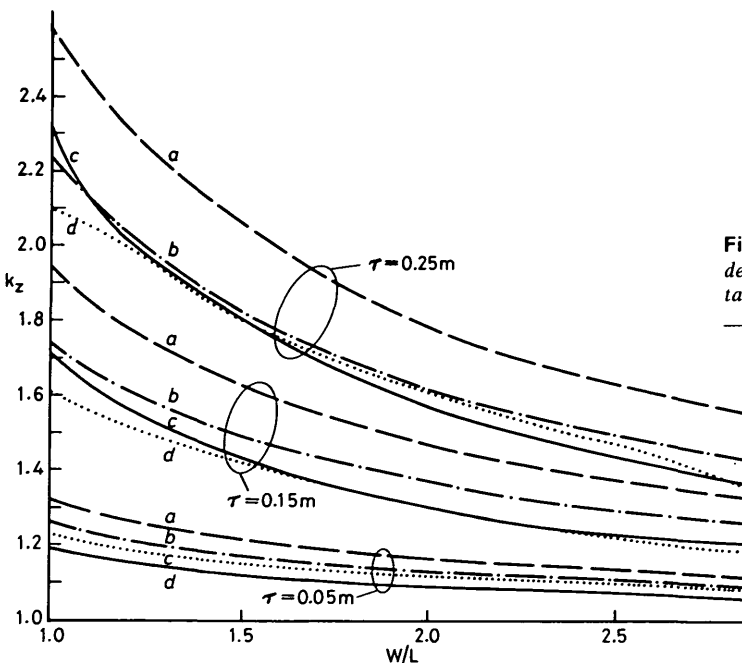
the saturation factor may be expressed by formula 26. The MMF of the airgap can be calculated on the basis of eqn. 5, i.e.

$$V_{gv} = \int_0^{g'} H_{mzv2} |_{x=0} \, dz$$

$$= \pm j \frac{A_{mv}}{M_v} \left[\mu_{re} \frac{\sinh (\beta_v g')}{\beta_v} - \frac{\kappa_{v1}}{\beta_v} \frac{1 - \cosh (\beta_v g')}{\beta_v} \right] \qquad (46)$$

To find the MMF of the solid secondary rail, one should first calculate the mean tangential flux

$$\Phi_{xvsec}(x) = w\mu_0 \, \mu_{rs} \int_{g'}^{\infty} H_{mxv2} \, dz \qquad (47)$$

The absolute value of magnetic flux is then

$$| \Phi_{xvsec}(x) | = w\mu_0 \frac{A_{mv}}{\beta_v} \frac{1}{|M_v|} \mu_{rs} \cos (\beta_v x)$$

The average value of magnetic field strength in the secondary of thickness h_{sec} is equal to

$$| H_{mxvav}(x) | = | \Phi_{xvsec}(x) | / (w h_{sec} \, \mu_0 \, \mu_{rav})$$

$$= \frac{1}{h_{sec}} \frac{A_{mv}}{\beta_v} \frac{1}{|M_v|} \frac{\mu_{rs}}{\mu_{rav}} \cos (\beta_v x) \qquad (48)$$

where μ_{rav} is the average relative magnetic permeability inside the interval $g' \leqslant z \leqslant g' + h_{sec}$. The MMF of the secondary along one pole pitch is then equal to

$$V_{secv} = \int_{-\tau/v}^{\tau/v} | H_{mxvav} | \, dx = \frac{1}{h_{sec}} \frac{2A_{mv}}{\beta_v^2} \frac{1}{|M_v|} \frac{\mu_{rs}}{\mu_{rav}} \qquad (49)$$

Expression 49, and the absolute value of expression 46, should now be put into relationship 26 for $v = 1$.
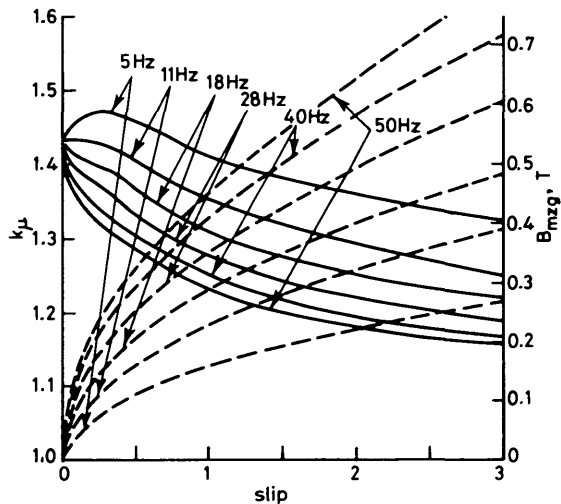
It can be seen from these considerations that the MMF

Fig. 13   Saturation factor k_μ and peak value of airgap magnetic flux density calculated for the CIGGT test SLIM (with longitudinal end effect taken into account)

——— B_{mzg}; - - - - k_μ

Fig. 12   Edge effect factors according to Gibbs [30], Panasienkov [33], Yee [34], and the authors

a Gibbs, b Panasienkov, c Yee, d the authors

of the solid-steel secondary depends on the z-co-ordinate, because of strong attenuation of the electromagnetic field inside the ferromagnetic conductive body. The saturation factor k_μ for the experimental machine is plotted as a function of slip in Fig. 13. Thrust/slip characteristics are very sensitive to saturation factor k_μ, particularly when $s > 0.3$. The relative magnetic permeability μ_{rs} at the surface of the solid-steel rail, as a function of slip, is shown in Fig. 14.

16.3 EMF across mutual reactance

The longitudinal end effect for a LIM with a solid-steel secondary is smaller than that for a LIM with a highly conductive cap over a ferromagnetic core, due to high impedance and high magnetic saturation of the solid-steel reaction plate. On the other hand, the influence of the end effect on the normal force is significant in the low slip range. In the range $0 < s < 0.35$, the end effect produces an EMF that weakens the airgap EMF ε (Fig. 14) generated

attenuation factor for the end-effect wave [36]*, and $f(\delta)$ is given by

$$f(\delta) = \frac{1}{T_e} \sin \delta + \frac{\pi}{\tau_e} \cos \delta \tag{52}$$

where δ is the phase angle between the normal travelling field and the end-effect wave at the front of the machine [36].

In this expression, the form factor σ_k of the EMF and the ratio of the average to the peak value of magnetic flux density α_i, are dependent on the saturation factor k_μ of the magnetic circuit. If $1 < k_\mu < 2$ then

$$\sigma_k \simeq \frac{\pi\sqrt{2}}{4} \exp\left(\frac{1 - k_\mu}{18}\right) \tag{53}$$

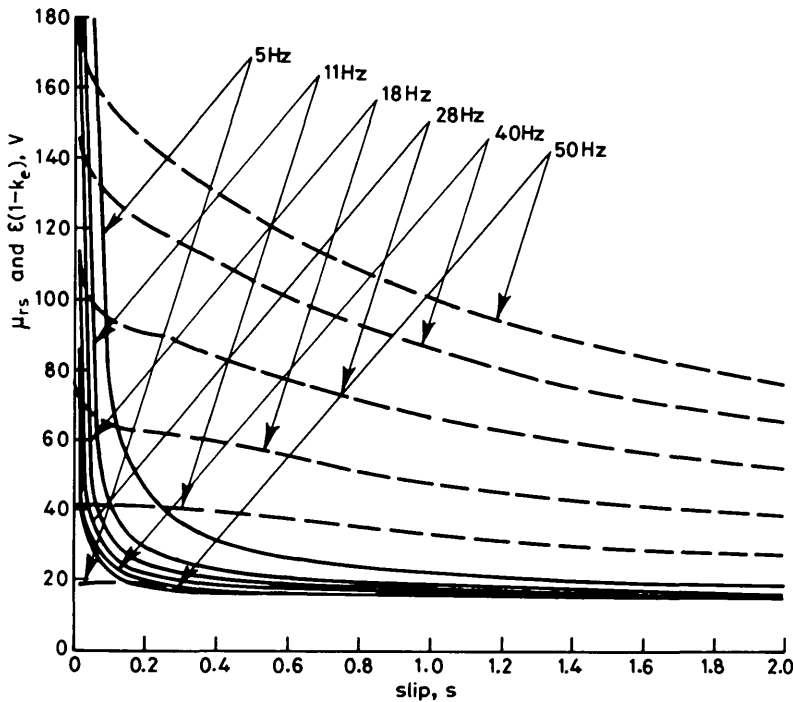$$\alpha_i \simeq \frac{2}{\pi} k_\mu^{1/3} \tag{54}$$

Fig. 14 *Surface relative magnetic permeability μ_{rs} and EMF $\varepsilon(1 - k_e)$ calculated for the CIGGT test SLIM (with longitudinal end effect taken into account)*

——— μ_{rs}; — — — $\varepsilon(1 - k_e)$

by the magnetic flux density wave travelling at synchronous velocity [35]. Consequently, the airgap magnetic flux density is equal to

$$B_{mg} = \frac{\varepsilon(1 - k_e)}{4\sigma_k \alpha_i N k_w f \tau L} \tag{50}$$

The correction factor $k_e < 1$ accounts for the longitudinal end effect and has the form*

$$k_e = -\frac{k_{we}}{k_w} \frac{\frac{\pi\tau_e}{\tau^2}}{\frac{1}{T_e^2} + \left(\frac{\pi}{\tau_e}\right)^2} f(\delta)e^{-p\tau_e/T_e} \frac{\sinh\left(\frac{p\tau_e}{T_e}\right)}{p \sinh\left(\frac{\tau_e}{T_e}\right)} \tag{51}$$

where τ_e, k_{we} and T_e are the pole pitch, winding factor and

To calculate the peak value B_{mg} of magnetic flux density in the airgap, the saturation factor k_μ has to be calculated first (Appendix 16.2). The EMF ε is then evaluated from the equivalent circuit (Fig. 2). The magnetic flux density obtained from eqn. 50 accounts for the longitudinal end effect.

According to Reference 25, the influence of the end effect on the thrust of a SLIM with a solid-steel reaction rail is negligible at $s > 0.3$, and small in the low slip range. The influence of the end effect on the normal force of a SLIM with a solid-steel secondary is greater than on the thrust (Figs. 5, 9 and 11).